aerospace

MDPI

Article

Computational Investigation of the Water Droplet Effects on Shapes of Ice on Airfoils

Andrey Kozelkov [1,2,3], Nikolay Galanov [1], Ilya Semenov [4], Roman Zhuchkov [1] and Dmitry Strelets [3,*]

1 Russian Federal Nuclear Center, All-Russian Research Institute of Experimental Physics, Nizhny Novgorod Region, Sarov 607188, Russia; askozelkov@mail.ru (A.K.)
2 Department of Applied Mathematics, Nizhny Novgorod State Technical University n.a. R.E. Alekseev, 24 ul. Minina, Nizhny Novgorod 603155, Russia
3 Aircraft Design and Certification Department, Moscow Aviation Institute, Volokolamskoe Shosse, 4, Moscow 125993, Russia
4 Department of Computational Mathematics, Federal State Institution "Scientific Research Institute for System Analysis of the Russian Academy of Sciences", Moscow 117218, Russia
* Correspondence: maksmai33@gmail.com

Abstract: The paper presents the results of studying the effects of droplet diameters on the NACA0012 airfoil ice accretion, which have been obtained in the 3D numerical simulation of icing. To simulate the motion of water droplets as a multiphase medium, the Eulerian approach is used, which assumes that water droplets have spherical shapes, do not undergo deformation and breakup, do not interact with each other, and that coalescence/fragmentation of droplets does not take place. Both monodisperse (of the same size) and polydisperse (of various sizes) droplets are considered; they are represented by the spectral Langmuir distributions. These spectral distributions take into account the polydisperse nature of droplets and provide a higher efficiency in predicting ice shapes. The obtained ice shapes on an airfoil are compared with the available experimental and calculated data. It should be noted according to the simulation results that the use of the standard size of droplet diameter equal to 20 µm does not allow for obtaining correct shapes of ice on the leading edge of the wing profile not at all temperature regimes. For temperatures from −20 °C to −10 °C, there is a noticeable difference compared to the experimental data. At the same time, for this temperature range, the use of the Langmuir spectral distribution of droplet diameters relative to 15 µm provides a better agreement of the formed ice forms with the experiment.

Keywords: ice accretion; airfoil; multiphase medium; monodisperse droplets; diameter; Langmuir distribution; temperature

Citation: Kozelkov, A.; Galanov, N.; Semenov, I.; Zhuchkov, R.; Strelets, D. Computational Investigation of the Water Droplet Effects on Shapes of Ice on Airfoils. *Aerospace* **2023**, *10*, 906. https://doi.org/10.3390/aerospace10100906

Academic Editor: Sergey Leonov

Received: 15 August 2023
Revised: 12 October 2023
Accepted: 15 October 2023
Published: 23 October 2023

1. Introduction

The numerical simulation, introduced as a stage of the design process to find optimum performance characteristics, allows for a reduction in design development time and cost, the scope of experimental investigations and flight tests, as well as simplifies the introduction of modifications to the design of air vehicles in the development stage [1,2]. The numerical simulation of ice accretion is an important aspect of the design process for ensuring the safety of aircraft, in particular, under cold weather conditions, where icing may cause serious problems [3,4]. Ice accretions on various surfaces may result in a lower airfoil lift force [5,6], a lower aerodynamic efficiency [7], and a lower visibility, thereby, complicating the air vehicle control for pilots. Experimental investigations reproducing ice accretion on solid surfaces of various aircraft are expensive, require much time, and do not allow studying the ice effect on the aerodynamic parameters of an aircraft in a short space of time [1]. Leading aerospace agencies in different countries are dealing with icing problems. The software developed by them or in cooperation with them allows to some extent modeling of icing processes. Currently, there are several codes that are most advanced in this issue:

- LEWICE (USA) [8];
- FENSAP-ICE (Canada) [9];
- CAPTA (France) [10];
- MULTIICE (Italy) [11];
- TRAJICE (UK) [12].

Icing on the aerodynamic surfaces of a body depends on a wide spectrum of the environment and body parameters [13]. Due to droplets impinging on a solid surface, a water film is generated on the surface and freezes at negative temperatures. To simplify the simulation of icing, the temperature of impinging droplets is taken equal to the incoming flow temperature. Temperature significantly affects the shape of ice. Small temperature differences may lead to large differences in ice shapes. With the environment temperature slightly exceeding 0 °C, icing is also possible because of a sudden change in the environmental parameters, such as a lower pressure. The environmental temperature of a typical ice cloud is −30 °C to 0 °C, according to the data from [14,15]. At negative temperatures of impinging droplets, two types of icing conditions are considered:

Complete icing is when all droplets impinging on a solid surface are transformed into ice (this paper does not consider supercooled water droplets freezing on surfaces [16–21]). Rime ice is formed under such conditions [22];

Partial icing is when ice and water film are on the surface at the same time. Glaze (or clear) ice is formed under such conditions [13].

The first type of icing is observed at a temperature of below −20 °C. There are no water films, and all water droplets impinging on a solid surface freeze and become rime ice or frost. The ice shape under such conditions replicates the airfoil shape. The icing takes place in the vicinity of the drag point and insignificantly influences the aircraft's aerodynamics [23]. Such ice is easily removed from the surface by an incoming flow, or due to vibrations, if a critical mass of ice has been formed, or if anti-icing devices are used. Figure 1 shows an example of ice under such icing conditions [22].

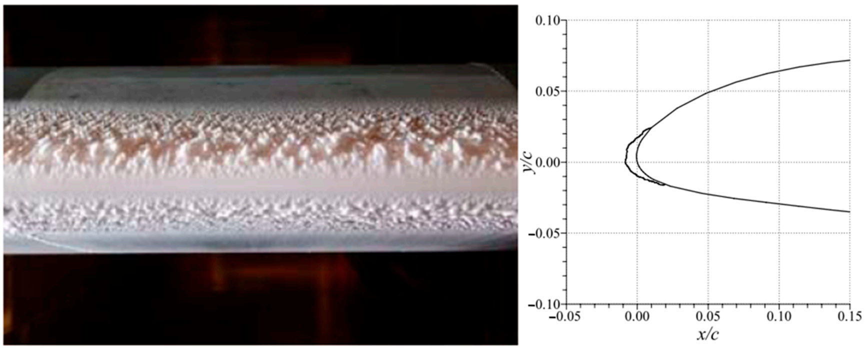

Figure 1. An example of rime ice on the leading edge of the wing.

The next type of icing condition is "partial" icing. The water film generated by droplets impinging on the solid surface partially freezes to form glaze ice and partially spreads over the surface owing to the incoming flow influence. A large portion of the water film spread over the surface freezes at a distance to the flow drag point and forms hornlike ice shapes, as shown in Figure 2.

Such type of icing is observed at the incoming flow temperatures from −20 °C to 0 °C. According to reference [13], this type of ice can be divided into two subtypes.

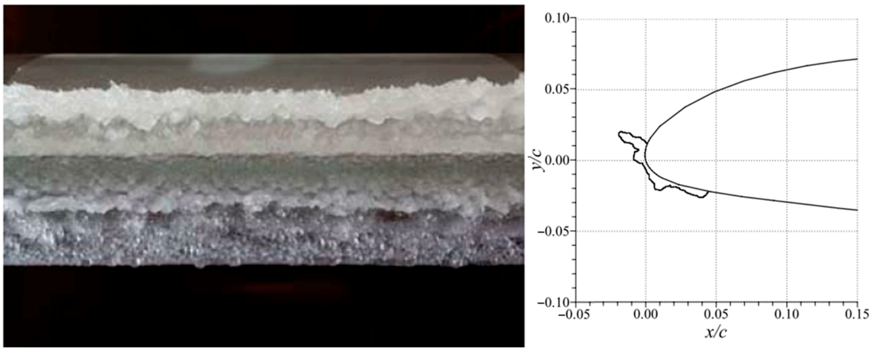

Figure 2. An example of glaze ice («horns») on the leading edge of a wing.

In the first case, a mixed ice (rime and glaze ice) is observed because supercooled droplets of various diameters are in the cloud [23]. This mixed ice is an intermediate ice shape between frost and glaze ice. Ice depositions resemble rime ice with ice feathers in the back part of the main ice shape. Such conditions cause safety risks because in the case of hornlike depositions significantly affecting the aircraft aerodynamics, the ice formed on the surface may separate due to the presence of rime ice and cause damage by hard pieces of ice.

The second subtype is completely clear ice with no rime ice structures. Such ice is formed at relatively high temperatures, from −10 °C to 0 °C [13]; it cannot be removed from the surface without the use of various anti-icing devices, which significantly affects the aerodynamic characteristics of an aircraft, and may cause serious consequences [23]. The aircraft's aerodynamic deteriorations are possible due to detached flow behind a hornlike ice deposition on the wing.

Note that at temperatures below −30 °C, supercooled water droplets have crystalline shapes in the cloud and being transported by air masses to the region of a higher temperature these crystals may melt and cause icing, if they adhere to the aerodynamic surface. Even in flights at an altitude of 12,000 m, where temperature may reach −40 °C, pilots observe ice crystal depositions on the aircraft windshield. Ice crystal depositions are possible on the blades of the propeller and inside of an engine nacelle. Various authors [24] conduct research in this area, which is important to ensure the safety of flights.

To study in detail the influence of various ice types on the aerodynamic characteristics of aircraft, it is necessary to properly simulate the physics of icing and the resultant shapes of ice depositions. In so doing, it is required to take into account constraints and the specifics of using the implemented models in numerical simulations. In particular, to simulate various ice shapes, the multistage approach [25] is required, which includes the stage of aerodynamic computations, the stage of simulating the water film spread over the model surface, the phase transition, and the icing simulation stage. In each stage, the method of iterations is used until the numerical solution convergence is achieved. The numerical simulation allows for studying in detail the ice formation.

2. Materials and Methods

This paper presents some mathematical models implemented in the Russian package of engineering analysis programs LOGOS, allowing numerical simulation of icing of various aircraft. The icing simulation method includes three stages. In the first stage, the 3D Navier–Stokes equation system is solved [26–30], which allows modeling the gas motion in the computational domain. In the second stage, the CFD simulation results are used to simulate the motion of supercooled water droplets as a continuum in the computational domain using the Eulerian approach [31,32]. In this paper, supercooled water droplets are understood as freezing fractions. The calculation of ice body size on the solid surface of the body of interest is the third stage in calculating the motion of water films. The morfing method [33] is used to change the object's surface shape depending on the amount of ice on the surface. The LOGOS software package version number 5.3.21 was comprehensively verified and validated on well-known international tests [1,34–38] and demonstrated good results. All the results given below were obtained using the LOGOS software package. The implemented methods of solving the icing problems allow us to reduce the cost of experimental investigations required to reveal the regularities in the formation of ice accretions and improve the accuracy of results.

2.1. Main Model Equations and the Numerical Solution Method

Unsteady 3D flows of a viscous gas with respect to heat transfer are described by the Reynolds Averaged Navier–Stokes equation system [27,28]; its conservative form in Cartesian coordinates can be written as follows (averaging symbols are omitted):

$$\begin{cases} \frac{\partial \rho}{\partial t} + \nabla\left(\rho \vec{u}\right) = 0, \\ \frac{\partial\left(\rho \vec{u}\right)}{\partial t} + \nabla\left(\rho \vec{u}\vec{u}\right) = -\nabla p + \nabla(\tau_\mu + \tau_t), \\ \frac{\partial(\rho E)}{\partial t} + \nabla\left(\rho \vec{u} h\right) = \nabla\left[\vec{u}(\tau_\mu + \tau_t) - \left(\vec{q}_\mu + \vec{q}_t\right)\right]. \end{cases} \tag{1}$$

The nomenclature used in the system of Equation (1): ρ is density; $\vec{u}$ is the flow velocity vector with components u, v, w; p is pressure; $E = C_v T + 0.5\left(u^2 + v^2 + w^2\right)$ is the total gas energy; $h = C_p T + 0.5\left(u^2 + v^2 + w^2\right)$ is the total gas enthalpy; τ_μ and τ_t are the molecular and turbulent components of the tangent stress tensor, respectively; q_μ and q_t are the molecular and turbulent components of the heat flux density, respectively; t is a time; $C_v = C_p - R/m$ is the specific heat capacity in constant volume; C_p is the specific heat capacity under constant pressure; R is a universal gas constant; m is the molar gas mass.

Values of the molecular component of the tangent stress tensor in Newton medium satisfy the rheological Newton law and are determined by the viscous stress tensor, and the strain rate [27,28,39] governs the relationship between the components of the heat flux density vector and the local temperature gradient:

$$\tau_\mu = 2\mu(T)\left(S - \frac{1}{3}I\nabla\vec{u}\right),\ S = \frac{1}{2}\left(\nabla\vec{u} + \left[\nabla\vec{u}\right]^t\right),\ q_\mu = \lambda(T)\nabla T \tag{2}$$

The dynamic viscosity coefficient $\mu(T)$ and the thermal conductivity coefficient $\lambda(T)$ depending on the heat flux temperature can be found using the Sutherland formula [40]:

$$\mu = \mu_0\left(\frac{T}{T_0}\right)^{0.5}\frac{T_0 + T_s}{T + T_s},\ \lambda = \lambda_0\left(\frac{T}{T_0}\right)^{0.5}\frac{T_0 + T_s}{T + T_s}, \tag{3}$$

where μ_0 and λ_0 are the dynamic viscosity and the thermal conductivity coefficients, respectively, at temperature T_0, and T_s is Sutherland constant.

The system of Equation (1) is not a closed system because of the unknown relation between the system variables τ_t and q_t the averaged flow parameters. To close the averaged system of equations, various models of turbulence are used. In the present paper, Equation (1) is closed using the two-parameter Menter model (SST) [41]. This model includes the transport equation for the turbulent kinetic energy and specific dissipation [41,42]. Linear differential models of turbulence use empirical relations for the turbulent viscosity coefficient, μ_t. Also, the Navier–Stokes equation system must be supplemented with boundary conditions of different types, and their description can be found in [43].

2.2. The Motion of Liquid Droplets as a Continuum in a Gas Dynamic Flow

In the Euler approach to calculating the water droplet distribution parameters in the computational domain in the carrying phase, the equation system consisting of the mass and momentum conservation equations is used [31,32]:

$$\begin{cases} \frac{\partial \alpha \rho_w}{\partial t} + \nabla \cdot \left(\alpha \rho_w \vec{u}_w \right) = 0 \\ \frac{\partial \alpha \rho_w \vec{u}_w}{\partial t} + \nabla \cdot \left(\alpha \rho_w \vec{u}_w \vec{u}_w \right) = \frac{f(\mathrm{Re}_r)}{\tau_p} \alpha \rho_w \left(\vec{u}_a - \vec{u}_w \right) + \alpha \rho_w \vec{F}_p \end{cases} \tag{4}$$

where α is the volume fraction of droplets, ρ_w is the droplet material density, $\vec{u}_a-$ is the carrying phase velocity (of the aerodynamic flow), and it can be found from system (1), $\vec{u}_w$ is the disperse phase velocity (of droplets), $\vec{F}_p$ is the external force per unit mass (for example, gravity force), and $f(\mathrm{Re}_r)$ is the droplet drag function:

$$f(\mathrm{Re}_r) = 1 + 0.15(\mathrm{Re}_r)^{0.687} + \frac{0.0175}{1 + \frac{4.25 \times 10^4}{(\mathrm{Re}_r)^{1.16}}} \tag{5}$$

Re_r is the algebraic Reynolds number:

$$\mathrm{Re}_r = \frac{\left| \vec{u}_a - \vec{u}_w \right| d_w}{\nu_a} \tag{6}$$

τ_p is the response time required to change the droplet velocity:

$$\tau_w = \frac{\rho_w d_w^2}{18 \mu_a} \tag{7}$$

ρ_w, d_w, ν_a, μ_a are the density and diameter of water droplets, the kinematic gas viscosity, and the dynamic gas viscosity, respectively.

This equation system models the parameters of water droplets moving in an airflow in the form of a disperse phase. Note that there is a unilateral connection between the gas medium and the flux of droplets, which is valid for the simulation of icing with a small ratio between the liquid and gas phases. Moreover, the following assumptions are used:

- All droplets are spherical, with no deformations and breakups of droplets.
- Droplets do not collide with each other, and coalescence/fragmentation of droplets does not take place.
- The effects conditioned by viscous forces are ignored.
- The drag and gravity forces act on droplets.

The first three items above are based on the fact that the disperse phase has no effect on the gas flow and the volume fraction of droplets in airflow is small. This model does not consider the droplet evaporation and condensation processes.

The system of Equation (4) is solved with the finite volume method (FVM) [44]. In this method, according to the geometric conservativeness principle, the system is reduced to the form:

$$\frac{d}{dt} \int_{\Omega} W dV + \oint_{\partial \Omega} \vec{F}^{*} dS = H \tag{8}$$

where $W = \begin{bmatrix} \alpha \\ \alpha u \\ \alpha v \\ \alpha w \end{bmatrix}$ is the vector of conservative variables; $u,\ v,\ w$ are the velocity vector components of a particle; $\overrightarrow{F}^{*} = \begin{bmatrix} \alpha(U_n - \dot{x}_n) \\ \alpha u(U_n - \dot{x}_n) \\ \alpha v(U_n - \dot{x}_n) \\ \alpha w(U_n - \dot{x}_n) \end{bmatrix}$ is flux; $\dot{x}_n = \left(\overrightarrow{\dot{x}},\ \overrightarrow{n}\right)$, $\overrightarrow{\dot{x}}$ is the velocity of a moving face of the control volume; H is the right-hand part vector.

This system must be supplemented with boundary conditions. In a general case, there are 3 main types of boundary conditions for the disperse phase: the inlet and outlet boundary conditions and an impermeable boundary. For the inlet and outlet boundaries, the Dirichlet boundary condition is used [45], and its parameters can be set as constants, functions, or tables. For the icing problems, the parameters used to solve the equation system include the carrying phase velocity and temperature, the volume fraction, and the diameter of droplets.

While setting the boundary conditions, the problematic part of the process is to properly calculate the parameters of water droplets impinging on a surface. In particular, the temperature of water droplets in the disperse phase that come into contact with a solid surface depends on the incoming flow temperature and velocity. In icing problems, it is assumed that any water droplet reaching the impermeable boundary is adsorbed on the surface, adheres to the surface, and forms a water film. The film thickness depends on the temperature of droplets impinging on the surface and the flow stagnation temperature [46]. In regions, where the flow separation from the wall is observed, such water film may not be created.

Ice accretions occur in the surface areas with a sufficient amount of water droplets. To identify such surface areas, the water droplet accumulation factor (β) is introduced, which characterizes the amount of water that has entered the given surface area and is limited in calculations by the limit from 0 to 1. As an example, Figure 3 geometrically illustrates the droplet accumulation factor on an airfoil for 2D (Figure 1 left) and 3D (Figure 1 right) cases. In a 2D case, this factor can be calculated as a ratio of the two distances: the distance between two droplets in the incoming flow (Δy_0) and the length of the arc on the airfoil formed by the same droplets, when they impinge on the surface (Δs). In a 3D case, the value of β factor is calculated as a ratio of the area occupied by droplets in the incoming flow (dy_0) to the droplet distribution area on the airfoil (ds).

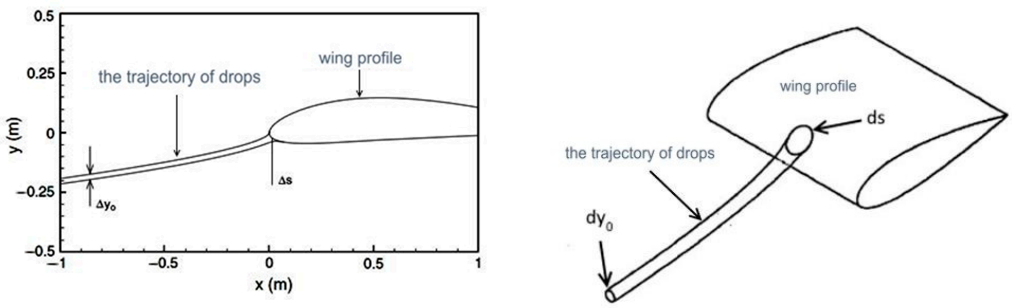

(**a**) (**b**)

Figure 3. Calculation of the liquid droplet accumulation factor on the airfoil surface for 2D (**a**) and 3D (**b**) cases.

So, the water droplet accumulation factor on the model surface is represented as follows [47]:

$$\beta = \frac{dy_0}{ds} \approx \frac{\Delta y_0}{\Delta s}, \tag{9}$$

where dy_0 is the distance between two droplets in an undisturbed flow, and ds is the length of the arc formed by the same droplets at points of impingement on the surface.

Such a way of calculating the accumulation factor for droplets from the disperse phase accumulated on a permeable surface causes difficulties in practice because of an extremely high computational load. To overcome such complications, the liquid droplet accumulation factor on the model surface can be found via the local mass flow of water on the model surface normalized to the product of the water velocity and mass fraction in the disperse phase on the input boundary [31]:

$$\beta = \frac{\alpha \rho_w u_i}{(LWC)U_\infty} \frac{S_i}{|S_i|} \tag{10}$$

where u_i is the averaged droplet velocity vector near face i, U_∞ is the liquid phase velocity amplitude on an open boundary, and S_i is the vector area of face i.

2.3. Calculation of Film Flows on Solid Surfaces

When calculating the liquid phase accumulation level (the water film formed on the solid surface), the mass, momentum, and temperature of droplets are also calculated and used in the liquid film motion equation based on the mass balance, the equation is as follows:

$$\dot{m}_V + \dot{m}_F = \dot{m}_d - \dot{m}_{evap} - \dot{m}_{ice} \tag{11}$$

where $\dot{m}_V = \rho_w \frac{\partial}{\partial t} \int\limits_S \int_0^{h_f} dy d\vec{x}$ is the rate of variations in the liquid water mass in the control volume;

$\dot{m}_F = \rho_w \int\limits_S div\left(\overline{u}_f\left(\vec{x}\right)h_f\right)d\vec{x}$ is the liquid water mass flow over the surface in the control volume;

$\dot{m}_d = \alpha_w \cdot \rho_w \cdot \left|\vec{u}_d\right|$ is the mass flow entering the control volume due to droplets impinging on the surface;

$\dot{m}_{evap} = \frac{0.7h_c}{c_{p,air}}\left[\frac{P_{v,p}(T) - H_{r,\infty}P_{v,\infty}}{P_\infty}\right]$ is the mass flow due to evaporation/sublimation;

$\dot{m}_{ice} = \int_S \dot{m}''_{ice}\left(\vec{x}, t\right)d\vec{x}$ is the mass flow leaving the control volume due to freezing;

where ρ_w is the water density;

S is the surface area;

h_f is the film height;

$\overline{u}_f$ is the moving film velocity in the direction $\vec{x}$;

$\vec{u}_d$ is the velocity of droplets impinging on the surface;

h_c is the thermal conductivity coefficient;

$P_{v,p}$ is the saturated vapor pressure on the surface;

$P_{v,\infty}$ is the saturated vapor pressure in the incoming flow;

P_∞ is the static pressure in the incoming flow;

$H_{r,\infty}$ is the relative humidity of surrounding air.

So, Equation (11) can be written in its conservative form:

$$\rho_w\left[\frac{\partial h_f}{\partial t} + \mathrm{div}\left(\overline{u}_f h_f\right)\right] = \dot{m}_d - \dot{m}_{evap} - \dot{m}_{ice} \tag{12}$$

For droplets impinging on a solid surface, the droplet distribution uniformity within the control volume over its lower surface is assumed. At the same time, the following assumptions are taken for the simplification purposes:

- there is no dissolved air in the liquid film;
- any air–water reaction is not taken into account;
- friction forces are the main driving factors for a liquid film;
- all properties are permanent inside the control volume of interest.

Figure 4 shows the heat transfer process components used to calculate the film flow on a solid surface.

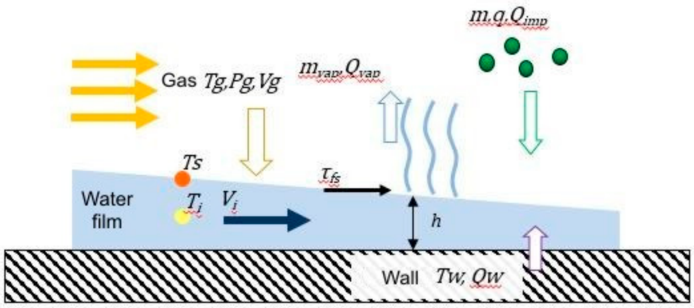

Figure 4. The main parameters used to calculate the film flow on a solid surface.

The heat transfer between droplets, film, and solid surface can be written in its general form as the energy conservation equation for the control volume:

$$\dot{Q}_V + \dot{Q}_F = \dot{Q}_d + \dot{Q}_{evap} + \dot{Q}_{ice} + \dot{Q}_{conv} + \dot{Q}_{cond} + \dot{Q}_{rad} \tag{13}$$

The liquid film moving through the control volume at a time t has temperature $\widetilde{T}\left(\vec{x}, t\right)$. The liquid film enthalpy is $c_{p,w}\widetilde{T}\left(\vec{x}, t\right)$. Hence, the film energy variation inside the control volume can be written as follows:

$$\dot{Q}_V = \frac{\partial}{\partial t}\int_S \left(\int_0^{h_f} \rho_w c_{p,w}\widetilde{T}\left(\vec{x}, t\right)dy\right)d\vec{x} = \int_S \frac{\partial}{\partial t}\rho_w c_{p,w} h_f\left(\vec{x}, t\right)\widetilde{T}\left(\vec{x}, t\right)d\vec{x} \tag{14}$$

The energy flux transported by the liquid film moving over the surface bounding the control volume is as follows:

$$\begin{aligned}\dot{Q}_F &= \int_{\partial S}\int_0^{h_f} \rho_w c_{p,w}\widetilde{T}\left(\vec{x}, t\right)\vec{u}_f\left(\vec{x}, y, t\right)\cdot\vec{n}\left(\vec{x}\right)dyd\vec{x} = \\ &= \rho_w\int_S div\left(\overline{u}_f\left(\vec{x}, t\right)h_f\left(\vec{x}, t\right)c_{p,w}\widetilde{T}\left(\vec{x}, t\right)\right)d\vec{x}\end{aligned} \tag{15}$$

Since droplets impinged on the surface become motionless after impingement, the drag enthalpy is used to calculate the energy of water falling onto the wall. The assumption of zero water enthalpy at freezing temperature T_0 = 0 °C is taken. The energy flux from impinging droplets is as follows:

$$\dot{Q}_d = \int_S \dot{m}_d\left(\vec{x}\right)\left[c_{p,w}(T_d - T_0) + \frac{\left|\vec{u}_d\right|^2}{2}\right]d\vec{x} \tag{16}$$

According to the Hedde approximation [46], during the evaporation/sublimation process, the first half of the water mass is considered to be in the liquid phase and the second half of it is in the solid phase. Such a simplified model takes into account that the liquid film on the ice surface is not continuous. As is evident from experimental observations, the liquid film on the body surface is separated by solid ice. In this case, ice is involved in the sublimation process, while the film is involved in the evaporation process. The energy flux resultant from these two processes can be written as follows:

$$\dot{Q}_{evap} = -\int_S \left[\frac{1}{2}(L_{evap}(T_0) + L_{sub}(T_0))\dot{m}_{evap}\right]d\vec{x} \tag{17}$$

where $L_{evap}(T_0)$ and $L_{sub}(T_0)$ are the specific heat of evaporation and sublimation, respectively.

The enthalpy of ice is calculated relative to its value for water at a freezing temperature of 0 °C. The energy flux leaving the control volume together with ice is as follows:

$$\dot{Q}_{ice} = \int_S \dot{m}_{ice}\left(\vec{x}, t\right)\left[L_{fus}(T_0) - c_{p,ice}\widetilde{T}\left(\vec{x}, t\right)\right] d\vec{x} \tag{18}$$

where $L_{fus}(T_0)$ is the specific heat of melting calculated at a temperature of freezing.

Heat losses due to the convective heat exchange with surrounding air have the form:

$$\dot{Q}_{conv} = \int_S \dot{Q}_{gas} d\vec{x} = \int_S \hat{k} \left.\frac{\partial \widetilde{T}_{air}}{\partial \vec{n}}\right|_{wall} d\vec{x} \tag{19}$$

where $\left.\frac{\partial \widetilde{T}_{air}}{\partial \vec{n}}\right|_{wall}$ is the temperature gradient on normal to the wall.

Flux $\dot{Q}_{gas}$ is transformed to the heat exchange coefficient prior to the calculation of icing:

$$h_c = \dot{Q}_{gas}/(T_{wall} - T^*) \tag{20}$$

where T^* is the film temperature.

The convective heat flux $h_c\left(\vec{x}\right)$ calculation is performed before each call to the gas solver. The heat flux value depends on temperature T^* of the boundary between gas and ice/film:

$$\dot{Q}_{conv} = \dot{Q}_h = h_c(T - T^*) \tag{21}$$

The following should be noted: The energy flux is mostly affected by the freezing heat; the second important quantity is the energy transferred by impinging droplets; the energy flux from the control volume mostly depends on the convective heat transfer and evaporation. On the background of all these factors, the prediction of a real ice shape depends, first of all, on the convective heat flux.

The rest quantities in Equation (13):

$\dot{Q}_{cond}$ is the heat flux transferred between water film and solid wall;

$\dot{Q}_{rad}$ is the radiative heat flux.

The following assumptions are used:

- ice is a heat insulator ($\dot{Q}_{cond} = 0$), and heat is not transferred between the wall and liquid film;
- there is no heat transfer between neighboring control volumes, and the energy exchange between them is due to the convective heat transfer only;
- a radiative heat flux is considered negligibly small, and its effect is significant, if only the simulation of anti-icing systems is performed ($\dot{Q}_{rad} = 0$).

In view of the aforesaid, the energy balance equation in its conservative form is as follows:

$$\begin{aligned} &\rho_w\left[\frac{\partial h_f c_{p,w}\widetilde{T}}{\partial t} + div\left(\overline{u}_f h_f c_{p,w}\widetilde{T}\right)\right] = \\ &= \left[c_{p,w}\widetilde{T}_d + \frac{\left|\vec{u}_d\right|^2}{2}\right]\dot{m}_d - 0.5\left(L_{evap} + L_{sub}\right)\dot{m}_{evap} + \left(L_{fus} - c_{p,ice}\widetilde{T}\right)\dot{m}_{ice} + \dot{Q}_h. \end{aligned} \tag{22}$$

To simulate the film state, the mass and energy balance equations are solved, the convection, evaporation, and sublimation processes are considered, and the film movement velocity is found on the base of tangent stresses on the surface:

$$\overline{u}_f = \frac{1}{h_f}\int_0^{h_f} \vec{u}_f\left(\vec{x}, y\right) dy = \frac{h_f}{2\mu_w}\vec{\tau}_{wall}\left(\vec{x}, y\right) \tag{23}$$

where $\vec{\tau}_{wall}$ are tangent stresses on the side of gas;

μ_w is the dynamic viscosity of water;

$h_f = \frac{\dot{m}_{evap}\Delta t}{\rho_w}$ is the generated film height.

Messinger's equations [47] are usually used when the movement of water films on a solid surface is not taken into account. However, to obtain smooth ice it is necessary to simulate a liquid film. In this work, modeling of liquid film flow and ice formation is based on solving the system of Equation (24) and consisting of the mass balance Equation (11) and energy (22).

$$\begin{cases} \rho_w \left[\frac{\partial h_f}{\partial t} + \mathrm{div}\left(\overline{u}_f h_f \right) \right] = \dot{m}_d - \dot{m}_{evap} - \dot{m}_{ice} \\ \rho_w \left[\frac{\partial h_f c_{p,w} \widetilde{T}}{\partial t} + div\left(\overline{u}_f h_f c_{p,w} \widetilde{T} \right) \right] = \\ = \left[c_{p,w} \widetilde{T}_d + \frac{\left| \vec{u}_d \right|^2}{2} \right] \dot{m}_d - 0.5\left(L_{evap} + L_{sub} \right) \dot{m}_{evap} + \left(L_{fus} - c_{p,ice} \widetilde{T} \right) \dot{m}_{ice} + \dot{Q}_h. \end{cases} \tag{24}$$

There are three unknowns in the system of Equation (24): film thickness h_f, equilibrium temperature of the air/film/ice/wall boundary $\widetilde{T}$, and mass flux due to icing $\dot{m}_{ice}$. Consequently, the above system requires additional relations-coexistence conditions. Based on experimental observations, they can be written as follows:

$$h_f \geq 0,\ \dot{m}_{ice} \geq 0,\ h_f \widetilde{T} \geq 0,\ \dot{m}_{ice} \widetilde{T} \leq 0 \tag{25}$$

According to the jointness conditions (25), the system of nonlinear Equation (24) is decomposed into three variants:

Variant I, $\dot{m}_{ice} = 0,\ h_f \geq 0,\ \widetilde{T} > 0$.

Variant II, $\widetilde{T} = 0,\ T = T_0,\ \dot{m}_{ice} > 0,\ h_f > 0$.

Variant III, $h_f = 0,\ \widetilde{T} < 0,\ \dot{m}_{ice} > 0,$.

For each option, a different system of nonlinear equations discretized by an explicit scheme is applied.

2.4. Geometry of the Motion of the Model Surface Faces

Ice accretions on surfaces lead to changes in the shape of boundaries. Changes in the shape of surfaces are accounted for by moving a face in the normal direction for walls with adhesion to the ice/film/multiphase flow interface, as shown in Figure 5.

Once the ice thickness $B(t)$ is calculated for each face, the displacement of each node of the surface mesh in the normal direction is calculated in a new time step using the formula:

$$d\vec{s}_i = \frac{\sum_{j=1}^{N} A_j B_j(t)}{\sum_{j=1}^{N} A_j} \vec{n}_i \tag{26}$$

where N is the number of faces to which a given node belongs;

A_j is the area of the face j;

B_j is the ice thickness on the face j;

$\vec{n}_i$ is normal to the surface at a point of surface i.

The computational mesh motion and deformation are independent components of the simulation process beyond the scope of the present paper. Different methods can be used to simulate the mesh deformation, and they are considered in detail in papers [48,49]. In the present paper, when representing the icing simulation results, the IDW (Inverse Distance Weighting) method [33,50] is used for the mesh model deformation.

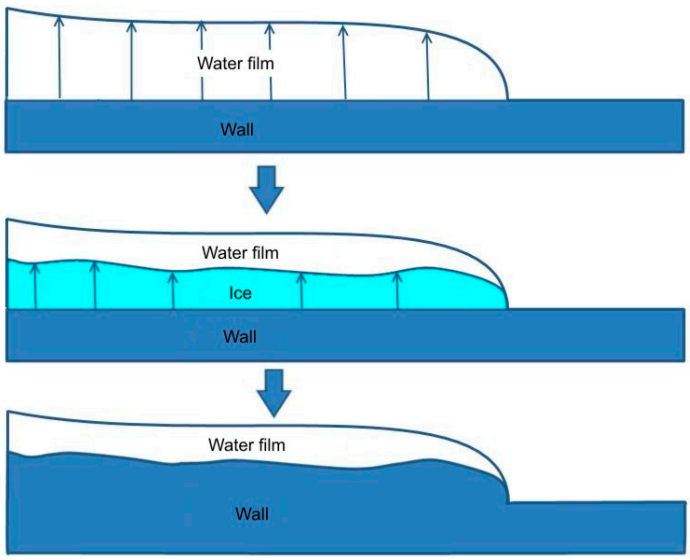

Figure 5. Changes in the impermeable boundary shape.

The models described above along with the assumptions have been implemented in the Russian LOGOS software package for the engineering analysis and allow simulation of the motion of liquid droplets as a disperse phase in a gaseous medium, as well as the generation of film on surfaces of the simulated body and spreading of these films over the surfaces. The calculated data are used to find the ice thickness and deform the ice-covered surface.

3. Results

This section will report the results collected from the model described in Section 2, Materials and Methods. In the first section, the ice accretion model has been validated with ice accreditation NACA0012 airfoil [51]; in the second section, the results of studying the effect of droplet diameter on icing will be presented. To perform verifications of the models presented in Section 2 and to enable further investigation of the effect of droplet diameters on icing, several computational geometries were constructed, which are necessary for the preliminary determination of the convergence of the solution by aerodynamic calculations. The computational models are unstructured quasi-two-dimensional meshes (one cell thick) consisting of truncated hexagons with five prismatic layers around the wing. The size of the prismatic cell was chosen from the condition y +< 30. Figure 6 shows the mesh models used in determining the convergence of the aerodynamic calculations. The number of cells in the presented models is 9000 (Figure 6a), 12,000 (Figure 6b), and 15,000 (Figure 6c), respectively.

All calculations were performed in parallel mode on 12 processors. A multistage approach consisting of step-by-step calculations was used for icing modeling. The first stage involved the calculation of gas dynamics and droplet motion of a continuous medium. In the second stage, the flow of the water film on the solid surface of the wing was calculated. In the third stage, the amount of ice formed and the movement of the computational model surface by the calculated ice height were calculated. All numerical calculations were performed without considering roughness. Each of the stages was carried out in turn one after another in the number of five steps. An implicit scheme was used for problem-solving. Convective flows were calculated according to the Roe scheme. The Mentor model (SST) was used to describe the turbulent characteristics. The convergence was evaluated using the distribution of the pressure coefficient on the wing at the first gas dynamic stage, the plot of which is shown in Figure 7. The graph shows the pressure coefficients on the wing profile for each computational model in comparison with the results of numerical calculations from [52].

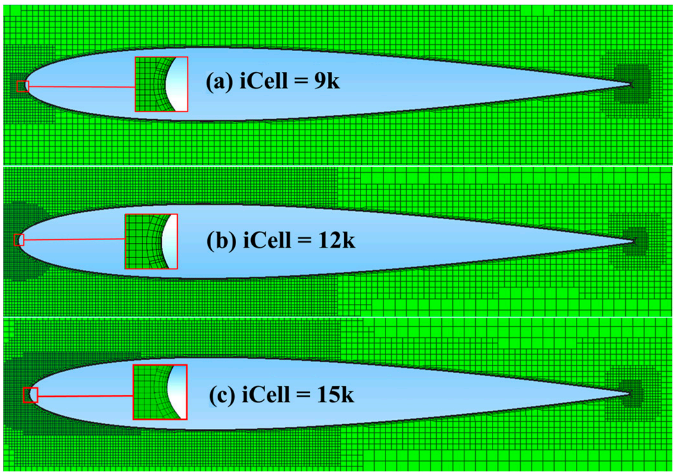

Figure 6. Mesh models used in the estimation of convergence of gas-dynamic calculations.

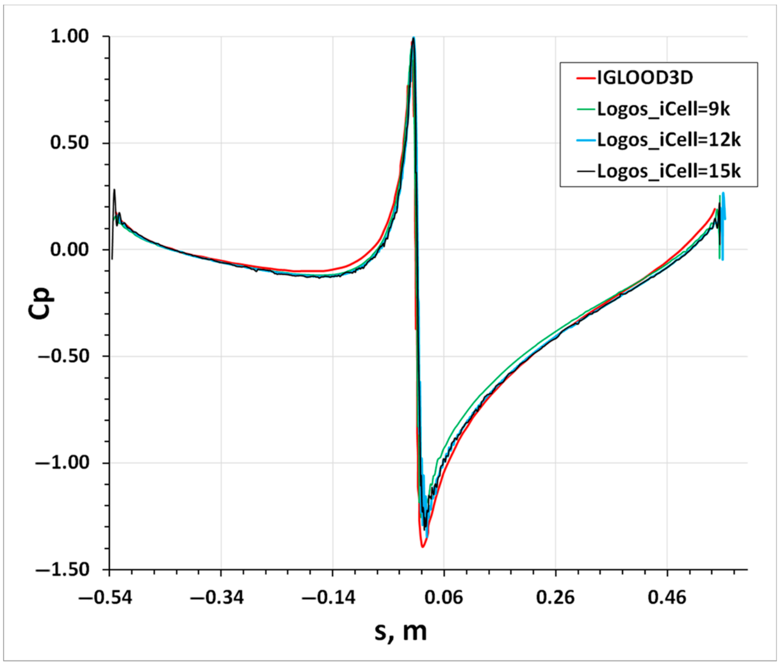

Figure 7. Graph of pressure coefficient distribution on the NACA0012 wing profile for different mesh models compared to results from [52].

According to the obtained data on the convergence of the solution, a computational model consisting of 15,000 cells was used in further calculations.

3.1. Ice Accretion Model Validation

Reference [51] presents the results of experimental investigations of the total temperature effects of an incoming flow on the ice formation and the ice formation effects on the aerodynamic characteristics of an airfoil. The total temperature is

$$T_{tot} = T_a + \frac{{U_a}^2}{2Cp_a} \tag{27}$$

where T_{tot} is the flow drag temperature (total temperature), T_a is the incoming flow (droplets) temperature, U_a is the incoming flow velocity, and Cp_a is the specific heat capacity of the incoming airflow.

Figure 8 shows one of the plots from [51], which represents the NACA0012 airfoil drag coefficient as a function of the total temperature.

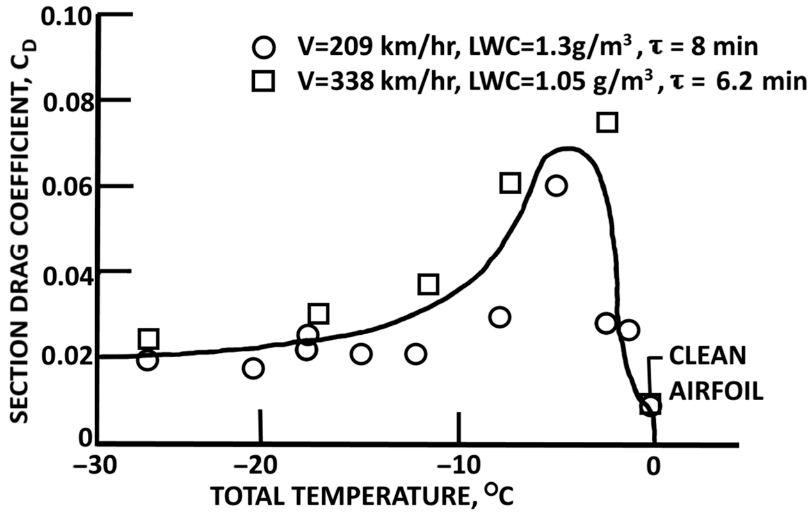

Figure 8. The NACA0012 airfoil drag coefficient as a function of the total temperature (Reprinted/adapted with permission from Ref. [51]. copyright AGARD 1997).

One can see from the plot above that with the total temperature of about −5 °C, the worst value of the NACA001 airfoil drag coefficient is observed under the following conditions: the incoming flow velocity V_1 = 209 km/h and V_2 = 338 km/h, the liquid water content LWC_1 = 1.3 g/m^3 and LWC_2 = 1.05 g/m^3, icing times t_1 = 8 min and t_2 = 6.2 min, and the attack angle of 3.5 degrees. This effect is conditioned by the influence of ice horns on the leading edge of the airfoil aerodynamics. Figure 9 shows different ice shapes at various values of the total temperature [51]. Also, Figure 9 shows hornlike growths formed at −5 °C.

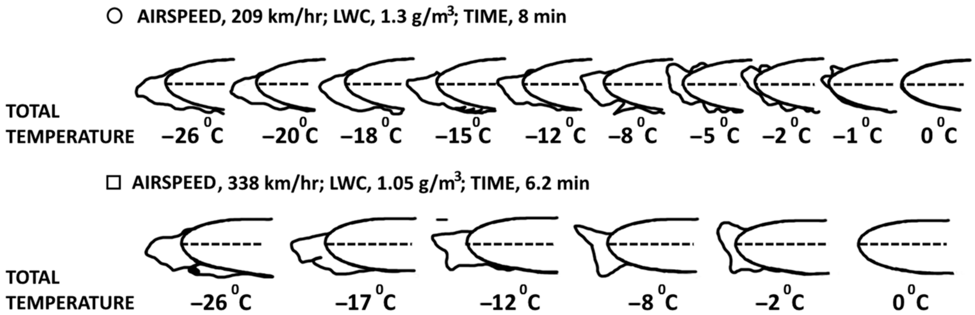

Figure 9. Ice shapes on a NACA0012 airfoil depending on the total temperature (Reprinted/adapted with permission from Ref. [51]. copyright AGARD 1997).

The results mentioned above clearly demonstrate the difference in ice shapes within a wide range of temperatures of the incoming flow; however, they do not make it possible to perform a qualitative comparison with the numerical simulation results, because the leading edge of the wing in [51] is given with ice depositions and not tied to the airfoil sizes. Some problems are formulated in [53], and the numerical simulation results and comparison with the experimental data from [51] are presented. Our paper describes the simulation of the icing process under the conditions from [53] given in Table 1.

Table 1. The icing process conditions for the numerical simulation.

Case No.	Experiment No.	T_a, °C	T_{tot}, °C
1	062791.009	−27.96	−26.28
2	062791.008	−21.96	−20.28
3	062791.007	−19.96	−18.28
4	062791.006	−16.96	−15.28
5	062791.005	−13.96	−12.28
6	062791.004	−9.96	−8.28
7	062791.001	−6.96	−5.28
8	062791.002	−3.96	−2.28
9	062791.003	−2.96	−1.28

Here, the experiment numbers are taken from [53]; T_a is the incoming flow temperature and the initial temperature of droplets; T_{tot} is the flow drag temperature.

Note that in [53], the quasi-two-dimensional mesh model was used for the numerical simulation. In our work, we also used the quasi-two-dimensional mesh model with the conditions from Table 1, and its parameters are given in Table 2.

Table 2. The parameters for the simulation of ice accretion on a NACA0012 airfoil.

Airfoil Name	Chord, m	V, m/s	P, Pa	α,°	LWC, kg/m^3	MVD, m	Icing Time, min
NACA0012	0.5334	58.1	90,760	3.5	1.3 × 10^3	20 × 10^6	8

Here, V is the flight velocity; P is pressure in an incoming flow; α is angle of attack; LWC is liquid water content; MVD is median volume diameter of droplets; icing time is the icing process duration.

The numerical simulation results for various ice shapes on the leading edge of the airfoil are compared with the experimental and numerical simulation results from [53] and shown in Figures 10–13.

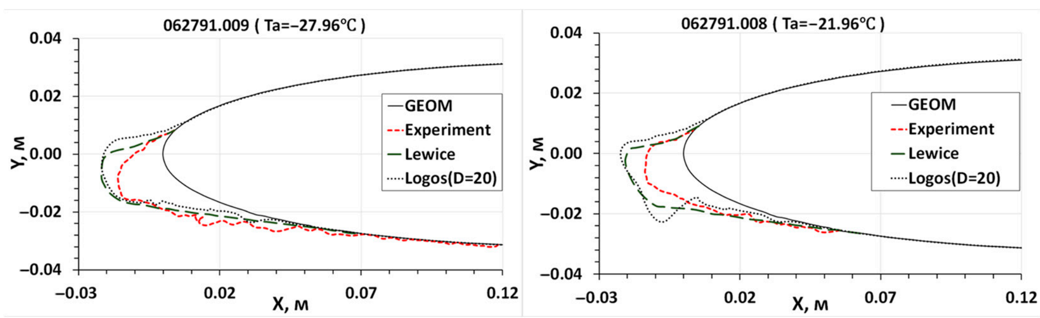

Figure 10. Comparison of ice shapes on the leading edge of the NACA0012 wing profile for Cases 1 (**left**) and 2 (**right**) from Table 1.

One can see from Figures 10 and 11 that all droplets impinging on the solid surface do not spread over the surface but are frozen at the flow drag point. Rime ice is formed at such temperatures. The main rime ice deposition is at the flow drag point and replicates the airfoil shape. The numerical simulation results demonstrate that a maximum ice height on the leading edge of the airfoil agrees with that obtained using Lewice [53]; however, the ice shapes differ from the experimental ones.

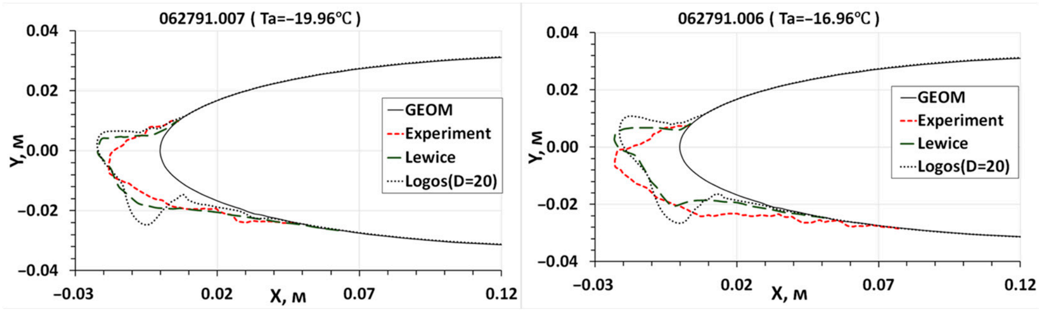

Figure 11. Comparison of ice shapes on the leading edge of the NACA0012 wing profile for Cases 3 (**left**) and 4 (**right**) from Table 1.

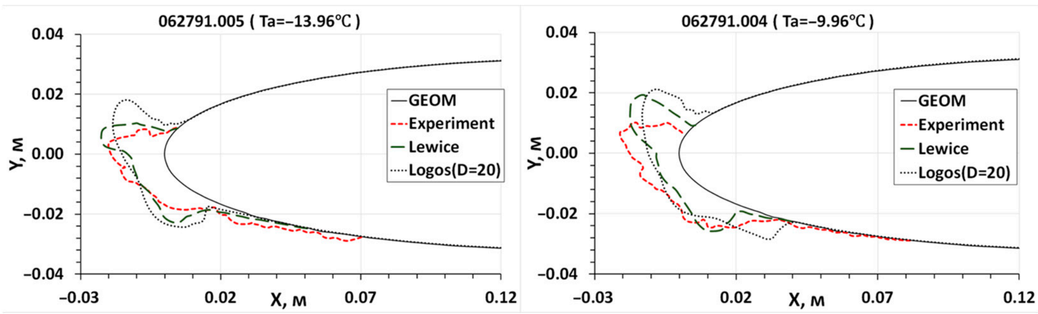

Figure 12. Comparison of ice shapes on the leading edge of the NACA0012 wing profile for Cases 5 (**left**) and 6 (**right**) from Table 1.

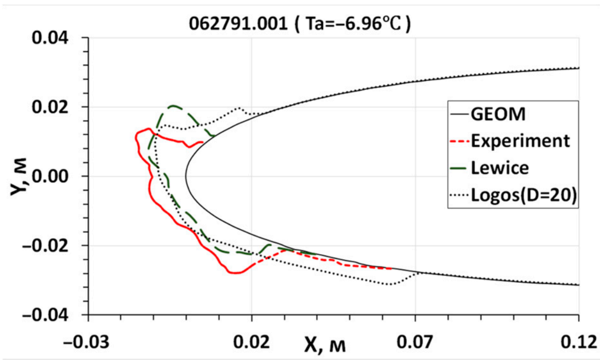

Figure 13. The iced NACA0012 airfoil shape: Case 7.

Figures 12 and 13 show the ice shapes on the airfoil for experimental conditions 5–7 from Table 1.

Figure 12 shows ice horns on the leading edge of the airfoil due to the spreading of the water film over the wing's leading edge surface in different directions from the stagnation point and freezing when the phase transition temperature is reached. The numerical simulation results differ from the available experimental data. Compared to the experiment, the horn-shaped ice deposition is more strongly shifted upstream from the flow braking point.

It can be seen in Figure 13 that the size of the "horn" obtained using numerical modeling starts to decrease as the braking temperature increases. At the same time, the water film spreads further away from the horn-shaped outgrowth and freezes. A similar uniform distribution of ice on the leading edge of the wing is shown in Figure 14. Thus, it should be noted that at temperatures above −10 °C, the heat flux has a fairly strong influence on the spreading and freezing of the water film on the wing surface. A small difference between the experimental heat flux and the flux obtained in numerical modeling can lead to large differences in the shapes of ice growths.

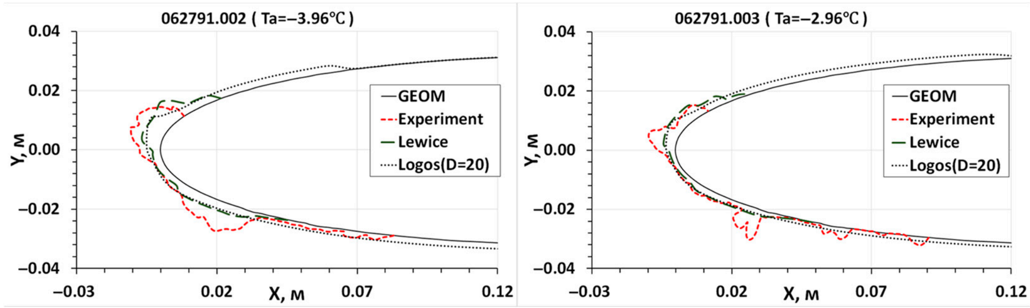

Figure 14. Comparison of ice shapes on the leading edge of the NACA0012 wing profile for Cases 8 (**left**) and 9 (**right**) from Table 1.

To analyze in detail the simulation results, Figures 15 and 16 show plots of the maximum ice height (H_{ice}) on the airfoil and the iced wing drag coefficient (C_{xa}) depending on the total temperature of the incoming flow.

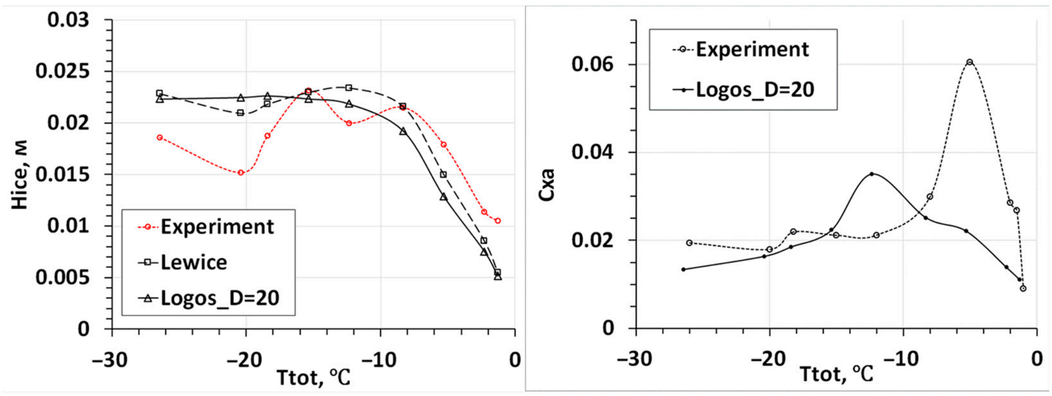

Figure 15. The ice height (**left**) and drag coefficient (**right**) as a function of the total temperature of the incoming flow for a NACA0012 airfoil.

According to the plots in Figure 15, one can conclude that the stable icing process on the airfoil is observed under experimental conditions 1–6 (Table 1) at temperatures below ∼−10 °C, and the formation of large ice depositions on the leading edge of the airfoil is typical at such temperatures. At temperatures above ∼−10 °C, the ice height starts decreasing; however, ice horns are formed, which have a significant effect on the aerodynamic characteristics of the airfoil. Such horns influence the airflow along the wing and may lead to an earlier stall of aircraft at smaller angles of attack. At environment temperatures higher than −10 °C, the ice mass and height start decreasing due to the water film spreading over the surface because of no film-to-ice phase transitions. In general, the transition from "complete" icing to "partial" icing is observed beginning from the incoming flow temperature of about −15 °C. This is also confirmed in papers [23,54]. According to the results from [51], the critical temperature of icing is within the range from −10 °C to −0 °C. In this temperature range, the ice shapes are formed, which significantly affects the foil aerodynamics. The numerical simulation results demonstrate that ice horns are formed at a temperature of −15 °C to −10 °C, and these results are contrary to the fact. There are several factors governing the difference between the calculated and experimental results. One of these factors is the size of water droplets impinging on the surface. So, in this connection, further research efforts are made.

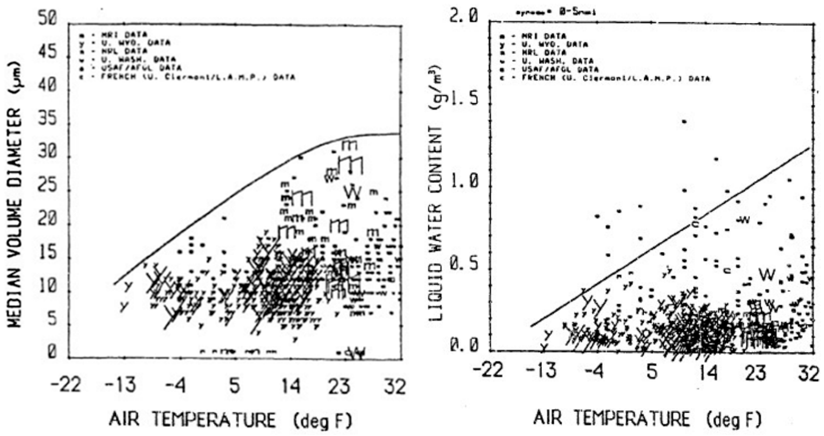

Figure 16. The median volume diameter (MVD) of supercooled water droplets in the cloud (**left**) and the liquid water content (**right**) as a function of the surrounding air temperature [13].

3.2. Studying the Droplet Diameter Effect on Icing

In most works on the simulation of icing on a NACA0012 airfoil [55,56], a monodisperse droplet flux with droplets of 20 μm in diameter is used. However, in the real world, water droplets in clouds are chaotically distributed and have different diameters. According to the authors (see, for example, [39]), the size of most supercooled water droplets ranges from 10 to 50 μm. However, Figure 16 taken from [13] illustrates the droplet MVD (median volume diameter) dependence on the surrounding air temperature. This parameter (MVD) is used for the median diameter of liquid supercooled droplets in clouds. Note that in the given experimental data [13], the diameter of droplets does not exceed 35 μm and decreases with a decreasing air temperature.

Also, super-cooled large droplets (SLDs) of 50 to 500 μm in diameter can be seen in the cloud [16–21]. Droplets of such diameters have significant effects on the aerodynamics of aircraft and, hence, on the safety of flights. The present paper does not consider SLDs and their effects because models are required to add them to the implemented code for the simulation of large droplets. The implemented code allows simulation of the effects of droplets of 10 μm to 50 μm diameters at various temperatures of the incoming flow. The diameters of water droplets can be set either using a monodisperse medium or their spectral distribution. For each experiment, the diameters of water droplets are the following: d = 10, 15, 20, 25, 30, 35, 40, 45, and 50 μm. Figures 17–21 show the ice shapes on the airfoil obtained with various diameters of water droplets.

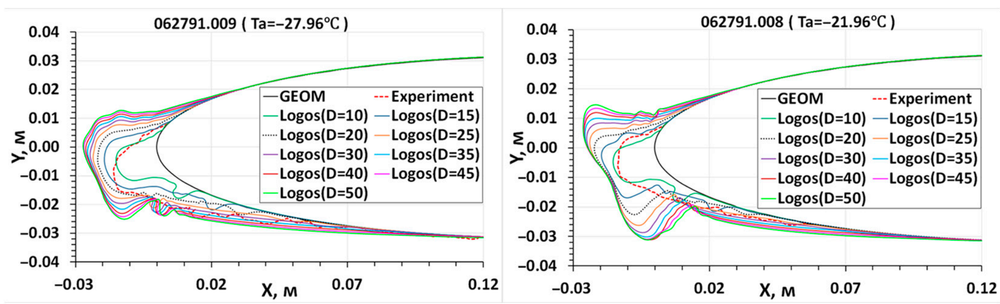

Figure 17. The iced NACA0012 airfoil shape: Cases 1 (**left**) and 2 (**right**).

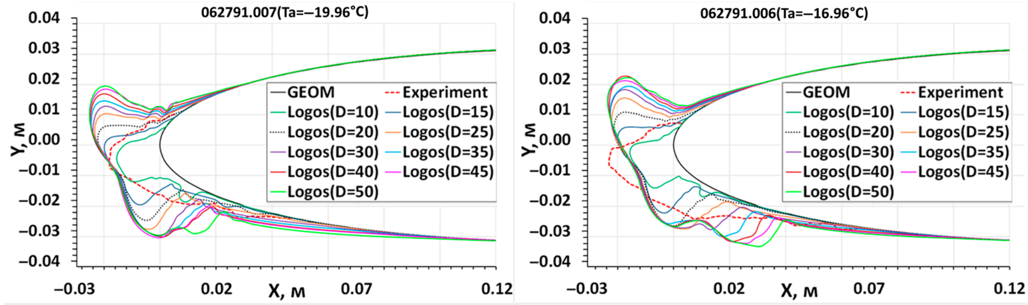

Figure 18. The iced NACA0012 airfoil shape: Cases 3 (**left**) and 4 (**right**).

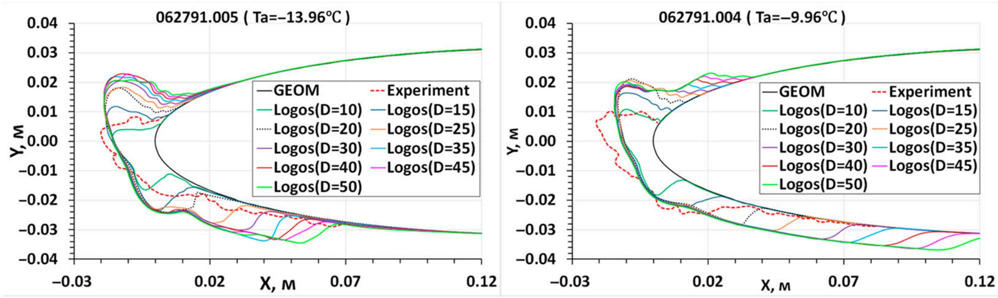

Figure 19. The iced NACA0012 airfoil shape: Cases 5 (**left**) and 6 (**right**).

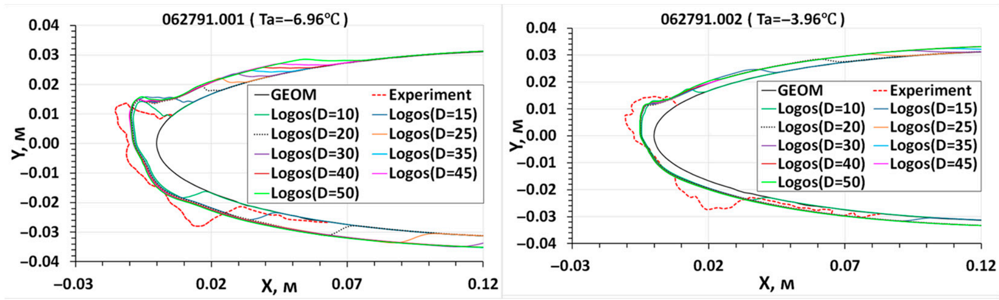

Figure 20. The iced NACA0012 airfoil shape: Cases 7 (**left**) and 8 (**right**).

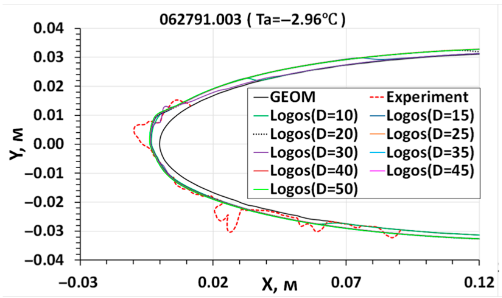

Figure 21. The iced NACA0012 airfoil shape: Case 9.

One can conclude, according to the results in Figures 17–21, that the size and shape of ice depositions on the leading edge of the airfoil depend on the diameters of water droplets in the incoming flow. With an increasing diameter of droplets, the amount of ice on the airfoil also increases. In this case, the increased diameter of droplets influences the area over which the water film spreads on the surface before it freezes. The larger the droplet diameter, the larger the distance of spreading. The ice thickness at the drag point is one and the same for all diameters of droplets. The height of the ice horn insignificantly changes with the increasing diameter of droplets. At temperatures higher than −5 °C, there are no ice horns on the leading edge of the wing and an increased diameter of droplets affects only the water film spread area before the film freezes.

Because of chaotically distributed droplets of different diameters in the cloud [19], the spectral distribution by droplet diameters and their fractions should be used to improve the accuracy of results in the numerical simulation of icing. Papers [57,58] proposed the weight coefficients for the distribution of the water droplet diameters and their fractions in the incoming flow, and these coefficients are given in Table 3.

Table 3. Coefficients of the droplet diameter distribution in spectra.

LWC Fraction	A	B	C	D	E	F	G	H	J
0.05	1.00	0.56	0.42	0.31	0.23	0.18	0.13	0.10	0.06
0.1	1.00	0.72	0.61	0.52	0.44	0.37	0.32	0.27	0.19
0.2	1.00	0.84	0.77	0.71	0.65	0.59	0.54	0.50	0.42
0.3	1.00	1.00	1.00	1.00	1.00	1.00	1.00	1.00	1.00
0.2	1.00	1.17	1.26	1.37	1.48	1.60	1.73	1.88	2.20
0.1	1.00	1.32	1.51	1.74	2.00	2.30	2.64	3.03	4.00
0.05	1.00	1.49	1.81	2.22	2.71	3.31	4.04	4.93	7.34

Table 3 presents the coefficients to obtain the water content of the flow (LWC) at the corresponding diameters. For example, having a droplet diameter of 20 µm and to obtain the droplet spectral distribution D from the table, we must multiply the droplet diameter by the coefficients in column D. Similarly, the water content is calculated. In paper [59], after the comparison between the numerical simulation results obtained using various Langmuir distributions by diameters of droplets and the available experimental icing data for a cylinder, the authors conclude that distributions B–E are the closest to reality. Using this data on the diameter distributions, the numerical simulations were performed for the experiments from Table 1. Figures 22–26 show the results obtained.

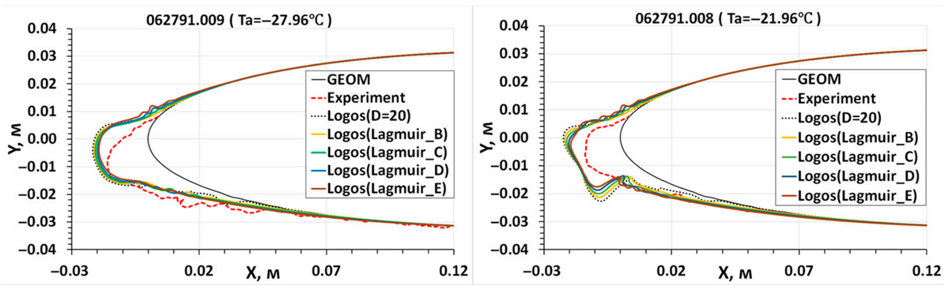

Figure 22. The iced shape of a NACA0012 airfoil: Cases 1 (**left**) and 2 (**right**).

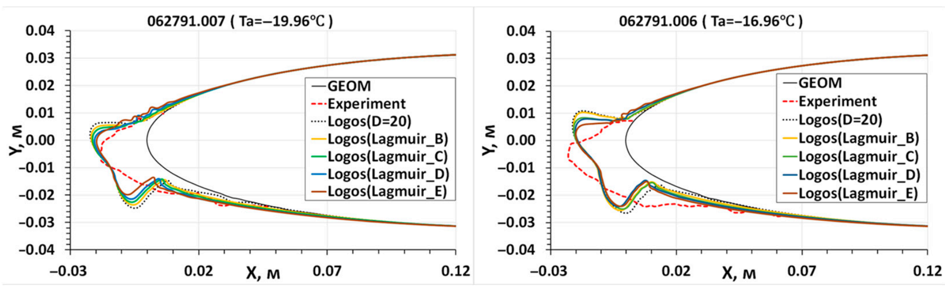

Figure 23. The iced shape of a NACA0012 airfoil: Cases 3 (**left**) and 4 (**right**).

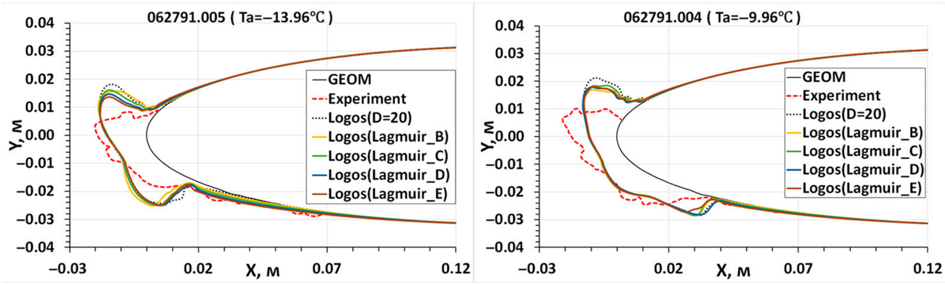

Figure 24. The iced shape of a NACA0012 airfoil: Cases 5 (**left**) and 6 (**right**).

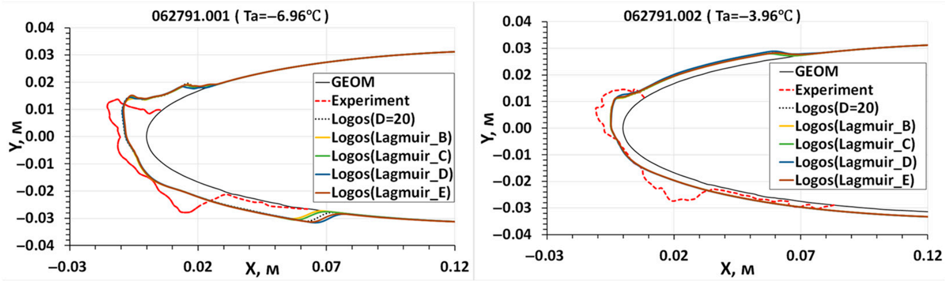

Figure 25. The iced shape of a NACA0012 airfoil: Cases 7 (**left**) and 8 (**right**).

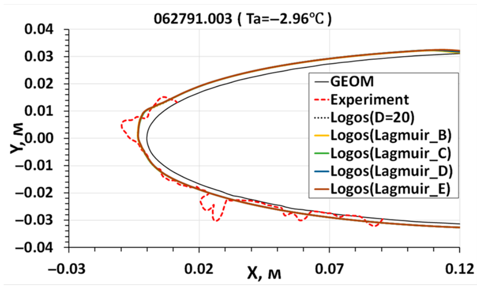

Figure 26. The iced shape of a NACA0012 airfoil: Case 9.

One can see in Figures 22–26 that with the use of the spectral Langmuir distributions of droplets having 20 µm diameters, the ice shapes on a NACA0012 airfoil slightly differ from the ice shapes obtained using a monodisperse medium with the same diameters of droplets.

The authors of the paper [13] demonstrate the dependence of 1000 experimentally measured median volume diameters (MVD) of water droplets on the liquid water content (LWC) in natural clouds. Figure 27 shows this data in comparison with the distributions from Appendix C to the US airworthiness standards FAR Part 25/29 [15]. According to Appendix C of US airworthiness standards FAR Part 25/29, droplet diameters are distributed between 15 µm and 40 µm. The remaining points in the graphs are data from [13].

It is evident from the comparison in Figure 27 that at different temperatures of surrounding air, the diameters of water droplets differ from those given in Appendix C to the US FAR Part 25/29 [15]. At low temperatures, in particular, the diameters of droplets do not exceed 15 µm. With an increasing temperature, the diameter of droplets agrees to some extent with the distributions from Appendix C; however, as we can see in Figure 27, most droplets have diameters of 10–15 µm. Results of simulations with various diameters of droplets show that with a droplet diameter of 15 µm, the ice shapes on the airfoil surface are close, to a high extent, to the experimental results. Additional calculations were made with the spectral Langmuir distribution of the water droplet diameters equal to 15 µm. The results obtained were compared with available data from experiments and the ice shapes obtained in the numerical simulation of problems with droplets 15 µm and 20 µm in diameter. Figures 28–32 show the comparison of the problem setups from Table 1.

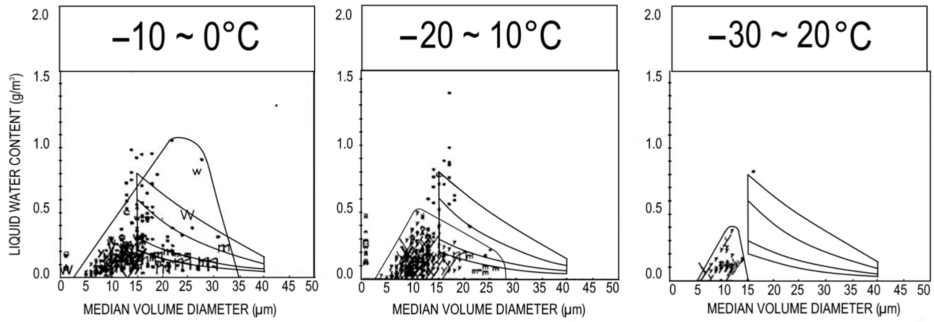

Figure 27. Comparison between the measured dependences of the liquid water content (LWC) on the median volume diameters (MVD) of water droplets with the distribution from Appendix C to the US FAR Part 25/29 [15].

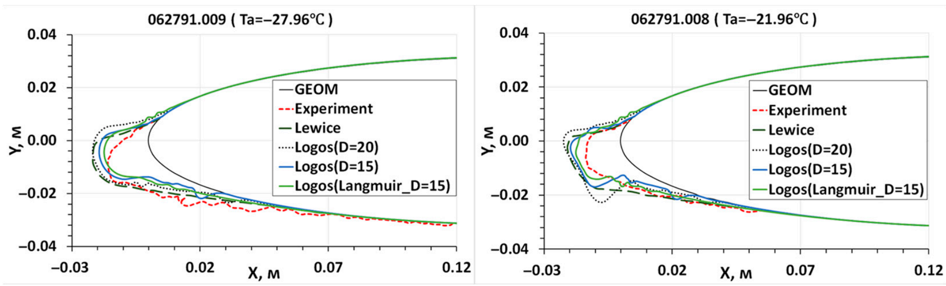

Figure 28. The iced shape of the NACA0012 airfoil: Cases 1 (**left**) and 2 (**right**).

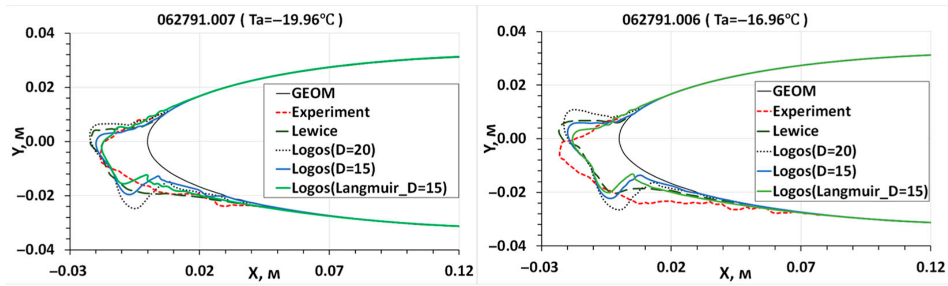

Figure 29. The iced shape of the NACA0012 airfoil: Cases 3 (**left**) and 4 (**right**).

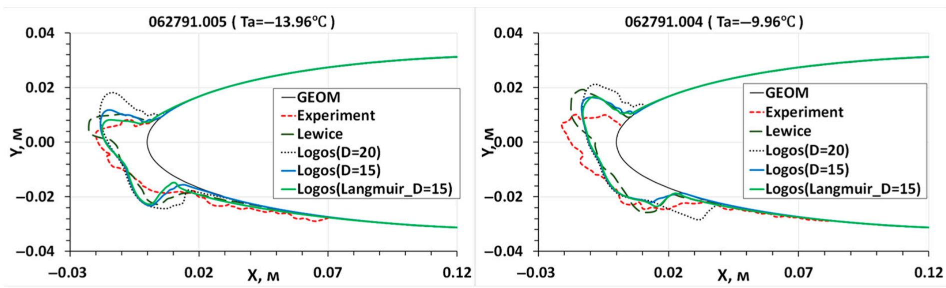

Figure 30. The iced shape of the NACA0012 airfoil: Cases 5 (**left**) and 6 (**right**).

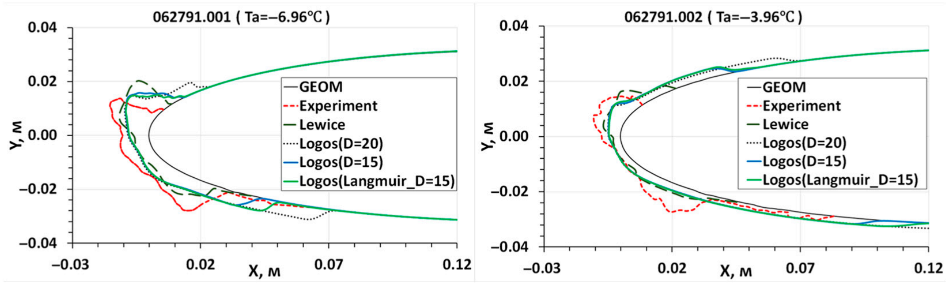

Figure 31. The iced shape of the NACA0012 airfoil: Cases 7 (**left**) and 8 (**right**).

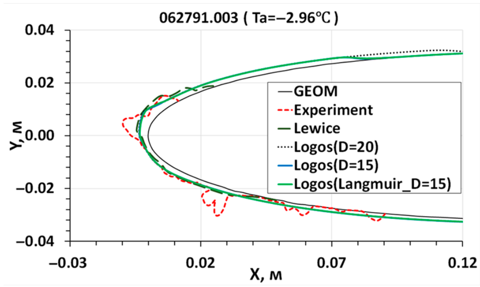

Figure 32. The iced shape of the NACA0012 airfoil: Case 9.

The numerical simulation results in Figures 28–32 demonstrate that in contrast to the ice shapes obtained in simulations with droplets having 20 µm diameters, the use of the Langmuir distribution of 15 µm diameter droplets allows us to obtain the ice shapes which qualitatively agree with those in the experiments. Langmuir distribution of droplets is not chaotic. However, it makes it possible to obtain results close to experimental data when calculating a quasi-two-dimensional (one-cell-width) computational model. The results can be assessed for temperatures of impinging droplets in the following way:

At temperatures below −20 °C, the ice shapes obtained in the numerical simulation agree with the results from [53] and insignificantly differ from the experiment.

At temperatures −20 °C to −10 °C, the obtained ice shapes are similar to those obtained by Lewice; however, the location of a hornlike ice deposition differs from the experimental one.

At temperatures above −10 °C, the ice height agrees with the experiment; however, additional formation of ice below the drag point and location of an ice horn is observed due to the water film spread and frozen on the wing surface.

Figure 33 shows the maximum height of ice (Hice) on the airfoil and the wing drag coefficient (Cxa) after icing as a function of the total temperature of the incoming flow.

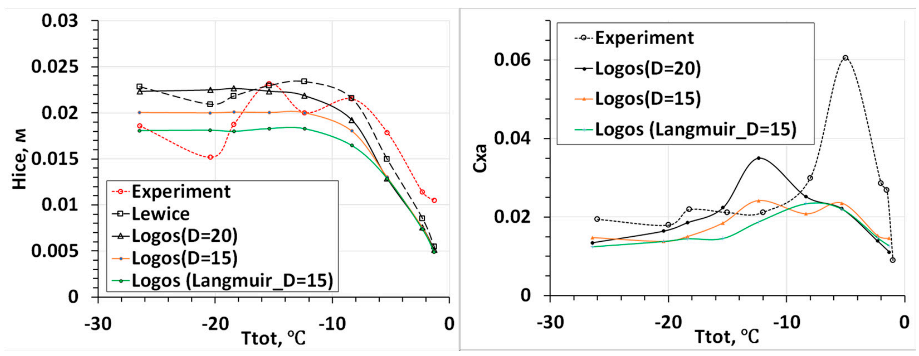

Figure 33. The ice height (**left**) on a NACA0012 airfoil and its drag coefficient (**right**) as a function of the total temperature of the incoming flow.

As one can see in Figure 33, the ice height (H_{ice}) on the airfoil when using the spectral Langmuir-D = 15 µm distribution of droplets differs from the numerical simulation results with droplets 20 µm in diameter at temperatures below −10 °C. However, in spite of this difference, the ice shapes obtained using the spectral Langmuir-D = 15 µm distribution of droplets are in better agreement with the experiment, and this is clearly seen in the plot of the drag coefficient distribution on the right-hand side of Figure 33. The use of the spectral distribution of droplets having diameters of about 15 µm at temperatures above −10 °C does not provide significant improvement in the numerical simulation results. The ice shapes are smoother than those in the experiment.

4. Conclusions

Possible errors and discrepancies in the experiment should be taken into account in the numerical simulation to correctly estimate the given parameters. It is also important to verify the implemented models using real data while taking into account the assumptions and constraints upon which these models are based the analysis of the simulation results has to be performed with regard to possible errors. The use of averaged data in the problem setup may lead to discrepancies in calculated and experimental results. In view of the fact that water droplets in natural clouds are chaotically distributed and have different diameters, it is a good practice to simulate the icing process using different diameters of droplets impinging on a body of interest, and this is proved by the results of the numerical studies presented in the paper. According to experimental data, the range of temperatures from −10 °C to 0 °C is critical for icing because hornlike ice shapes are formed and have significant effects on the aerodynamic characteristic of an aircraft wing. The numerical simulation results in this range of temperatures demonstrate the difference in the location of ice on the leading edge of the airfoil. To obtain the numerical simulation results, which are in better agreement with the experiment, additional efforts in studying the ice formation at such temperatures are required to understand the effect of

- turbulence and roughness of the iced surface of a 3D airfoil on its aerodynamic characteristics;
- the spread water film separation from the surface under the influence of the incoming flow;
- splashing of water droplets impinging on a solid surface and later frozen on the surface.

Most authors in numerical modeling of icing of aerodynamic objects use a fixed droplet diameter and do not indicate in which regimes, when using the Langmuir distribution, it is possible to obtain a positive effect, for example, the shapes of ice outgrowths that better match the experimental data. In this work, it was found that the use of Langmuir distributions in droplet modeling is justified at certain temperature regimes, which was not considered in the studied works presented in the reference list. According to the presented results, it is recommended to use fixed values of droplet diameters in numerical modeling to obtain ice growth forms close to the experimental ones at temperatures below −20 °C and above −10 °C. At temperatures between −20 °C and −10 °C, the use of Langmuir distributions with droplet diameters of 15 µm gives better agreement of ice growth shapes on the wing profile than monodisperse droplets with diameters of 20 µm. The icing process has complex physics. Further development of and modifications to the implemented methods and approaches would allow for improving the numerical simulation results to make it possible for engineers to analyze in the design stage the icing effects on the aerodynamic characteristics of aircraft.

Author Contributions: Conceptualization, A.K. and N.G.; methodology, A.K. and I.S.; software, A.K.; validation, R.Z., D.S.; formal analysis, A.K. and D.S.; investigation, I.S.; writing—original draft preparation, N.G. and R.Z.; writing—review and editing, R.Z.; visualization, D.S. All authors have read and agreed to the published version of the manuscript.

Funding: The work was supported by the Program for Creation and Development of World-Class Scientific Center "Supersonic" in 2020–2022 with financial support from the Russian Ministry of Education and Science (Agreement No. 075-15-2020-924 dated 16.11.2020). The results have been obtained with financial support from the Science and Universities National Project under the Young Scientists Lab Program of the RF Ministry of Education and Science—project identifier No. FSWE-2021-0009 (Research Topic: Development of CFD methods, models and algorithms to simulate liquids and gases in natural and industrial environments under normal and critical conditions on petascale supercomputers) and the Council of the Grants of the President of the Russian Federation for state support of Leading Scientific Schools of the Russian Federation (Grant No. NSH-70.2022.1.5).

Data Availability Statement: Not applicable.

Conflicts of Interest: The authors declare no conflict of interest.

References

1. Kozelkov, A.S.; Pogosyan, M.A.; Strelets, D.Y.; Tarasova, N.V. Application of mathematical modeling to solve the emergency water landing task in the interests of passenger aircraft certification. *Aerosp. Syst.* **2021**, *4*, 75–89. [CrossRef]
2. Kind, R.J.; Potapczuk, M.G.; Feo, A.; Golia, C.; Shah, A.D. Experimental and computational simulation of in-flight icing phenomena. *Prog. Aerosp. Sci.* **1998**, *34*, 257–345. [CrossRef]
3. Lynch, F.T.; Khodadoust, A. Effects of ice accretions on aircraft aerodynamics. *Prog. Aerosp. Sci.* **2001**, *37*, 669–767. [CrossRef]
4. Cao, Y.H.; Tan, W.Y.; Wu, Z.L. Aircraft icing: An ongoing threat to aviation safety. *Aerosp. Sci. Technol.* **2018**, *75*, 353–385. [CrossRef]
5. Myers, T.G.; Charpin, J.P.F. A mathematical model for atmospheric ice accretion and water flow on a cold surface. *Int. J. Heat Mass Transf.* **2004**, *47*, 5483–5500. [CrossRef]
6. Kong, W.; Liu, H. A theory on the icing evolution of supercooled water near solid substrate. *Int. J. Heat Mass Transf.* **2015**, *91*, 1217–1236. [CrossRef]
7. Cao, Y.; Huang, J.; Yin, J. Numerical simulation of three dimensional ice accreation on an aircraft wing. *Int. J. Heat Mass Transf.* **2016**, *92*, 34–54. [CrossRef]
8. Ruff, G.A.; Berkowitz, B.M. Users Manual for the Improved NASA Lewis Ice Accretion Code LEWICE 1.6; NASA-CR-198355 1990.
9. Bourgault, Y.; Beaugendre, H.; Habashi, W.G. Development of a Shallow-Water Icing Model in FENSAP-ICE. *J. Aircr.* **2000**, *37*, 640–646. [CrossRef]
10. Hedde, T.; Guffond, D. ONERA Three-Dimensional Icing Model. *AIAA J.* **1995**, *33*, 1038–1045. [CrossRef]
11. RIuliano, T.E.; Brandi, V.; Mingione, G.; de Nicola, C. Water impingement prediction on multi-element airfoils by means of Eulerian and Lagrangian approach with viscous and inviscid air flow. In Proceedings of the 44th AIAA Aerospace Sciences Meeting and Exhibit, Reno, NV, USA, 9–12 January 2006; p. 1270.
12. Gent, R.W. TRAJICE2—A Combined Water Droplet Trajectory and Ice Accretion Prediction Program for Aerofoils. RAE TR 90054. 1990. Available online: https://ntrs.nasa.gov/api/citations/19970023937/downloads/19970023937.pdf (accessed on 24 March 2023).
13. Han, Y. Theoretical and Experimental Study of Scaling Methods for Rotor Blade Ice Accretion Testing. Doctoral Dissertation, The Pennsylvania State University, State College, PA, USA, August 2011. [CrossRef]
14. Federal Aviation Regulations. *Part 25 Airworthness Standards: Transport Category Airplanes*, 3rd ed.; with amendments 1–7. JSC «AVIAIZDAT»; 2014. Available online: https://www.ecfr.gov/current/title-14/chapter-I/subchapter-C/part-25 (accessed on 24 March 2023).
15. FAA. *Federal Aviation Regulation, Part 29 (FAR 29), «Airworthiness Standarts:Transport Category Rotorcraft», Appendix C, (Code of Federal Regulations, Title 14, Chapter 1, Part 29, Appendix C), Superintendent of Documents*; Government Printing Office: Washington, DC, USA, 1994; p. 20402.
16. Honsek, R.; Habashi, W.G. FENSAP-ICE: Eulerian Modeling of Droplet Impingement in the SLD Regime of Aircraft Icing. In Proceedings of the 44th AIAA Aerospace Sciences Meeting and Exhibit, Reno, NV, USA, 9–12 January 2006.
17. Honsek, R.; Habashi, W.G.; Aub'e, M.S. Eulerian Modeling of In-Flight Icing Due to Supercooled Large Droplets. *J. Aircr.* **2008**, *45*, 1290–1296. [CrossRef]
18. Rocco, E.T.; Han, Y.; Palacios, J. Super-cooled Large Droplet Ice Accretion Reproduction and Scaling Law Validation. In Proceedings of the 8th AIAA Atmospheric and Space Environments Conference, AIAA Aviation, Washington, DC, USA, 13–17 June 2016.
19. Wright, W.; Potapczuk, M. Semi-Empirical Modelling of SLD Physics. In Proceedings of the 42nd AIAA Aerospace Sciences Meeting and Exhibit, Reno, NV, USA, 20 January 2004.
20. Bilodeau, D.; Habashi, W.G.; Fossati, M. Numerical Modeling of Supercooled Large Droplets Re-impingement. In Proceedings of the 21st Annual Conference of the CFD Society of Canada, Sherbrooke, QC, Canada, 6 May 2013.
21. Jung, S.K.; Kim, J.H. Numerical Model for Eulerian Droplet Impingement in Supercooled Large Droplet Conditions. In Proceedings of the 51st AIAA Aerospace Sciences Meeting including the New Horizons Forum and Aerospace Exposition, Grapevine, TX, USA, 7–10 January 2013. AIAA-2013-0244.

22. Bragg, M.B.; Broeren, A.P.; Addy, H.E.; Potapczuk, M.G.; Guffond, D.; Montreuil, E. Airfoil Ice-Accretion Aerodynamics Simulation, AIAA–2007–0085. In Proceedings of the 45th Aerospace Sciences Meeting and Exhibit sponsored by the American Institute of Aeronautics and Astronautics, Reno, NV, USA, 1–8 January 2007.
23. Alekseyenko, S.V.; Prykhodko, A.A. Numerical simulation of icing on a cylinder and an airfoil: Model review and computational results. *TsAGI Sci. J.* **2013**, *XLIV*, 25–57. [CrossRef]
24. Amelyushkin, I.A. Study of Two-Phase Flows in Application to Icing Problems and Aerophysical Experiment. Ph.D. Thesis, Central Aerohydrodynamic Institute (TsAGI), Moscow, Russia, 2014.
25. Galanov, N.G.; Sarazov, A.V.; Zhuchkov, R.N.; Kozelkov, A.S. Application of various ice accretion simulation approaches in the LOGOS software package. In Proceedings of the Journal of Physics: Conference Series, Volume 2099, International Conference «Marchuk Scientific Readings 2021» (MSR-2021), Novosibirsk, Russia, 4–8 October 2021; p. 012029. [CrossRef]
26. Fletcher, C. *Computational Techniques for Fluid Dynamics*; Springer: Berlin/Heidelberg, Germany, 1988; Volume 2.
27. Landau, L.D.; Lifshits, E.M. Theoretical physics. In *Hydrodynamics*; Nauka: Moscow, Russia, 1988; Volume VI.
28. Loitsyanskii, L.G. *Mechanics of Liquids and Gases*; Nauka: Moscow, Russia, 1979.
29. Kovenya, V.M.; Babintsev, P.V. Application of splitting algorithms in the method of finite volumes for numerical solution of the Navier–Stokes equations. *J. Appl. Industr. Math.* **2018**, *12*, 479–491. [CrossRef]
30. Kovenya, V.M. Splitting algorithms for numerical solution of Navier–Stokes equations in fluid dynamics problems. *Prikl. Mekh. Tekh. Fiz.* **2021**, *62*, 48–59.
31. Kim, J.W.; Dennis, P.G.; Sankar, L.N.; Kreeger, R.E. Ice Accretion Modeling using an Eulerian Approach for Droplet Impingement. In Proceedings of the 51st AIAA Aerospace Sciences Meeting including the New Horizons Forum and Aerospace Exposition, Grapevine, TX, USA, 7–10 January 2013.
32. Norde, E. Eulerian Method for Ice Crystal Icing in Turbofan Engines. Ph.D. Thesis, University of Twente, Enschede, The Netherlands, 2017. [CrossRef]
33. Luke, E.; Collins, E.; Blades, E. A fast mesh deformation method using explicit interpolation. *J. Comp. Phys.* **2012**, *231*, 586–601. [CrossRef]
34. Kozelkov, A.S.; Struchkov, A.V.; Strelets, D.Y. Two Methods to Improve the Efficiency of Supersonic Flow Simulation on Unstructured Grids. *Fluids* **2022**, *7*, 136. [CrossRef]
35. Struchkov, A.V.; Kozelkov, A.S.; Zhuchkov, R.N.; Volkov, K.N.; Strelets, D.Y. Implementation of Flux Limiters in Simulation of External Aerodynamic Problems on Unstructured Meshes. *Fluids* **2023**, *8*, 31. [CrossRef]
36. Korotkov, A.; Kozelkov, A. Three-dimensional numerical simulations of fluid dynamics problems on grids with nonconforming interfaces. *Sib. Electron. Math. Rep.* **2022**, *19*, 1038–1053. [CrossRef]
37. Kozelkov, A.; Kurkin, A.; Kurulin, V.; Plygunova, K.; Krutyakova, O. Validation of the LOGOS Software Package Methods for the Numerical Simulation of Cavitational Flows. *Fluids* **2023**, *8*, 104. [CrossRef]
38. Oran, E.; Boris, J. *Numerical Simulation of Reactive Flow*; Cambridge University Press: Cambridge, UK, 2001.
39. Schlichting, G. *Theory of the Boundary Layer*; Nauka: Moscow, Russia, 1974; 712p.
40. Menter, F.R. Zonal two–equation k–w turbulence models for aerodynamic flows. In Proceedings of the 23rd Fluid Dynamics, Plasmadynamics, and Lasers Conference, Orlando, FL, USA, 6–9 July 1993; p. 2906.
41. Garbaruk, A.V.; Strelets, M.K.; Travin, A.K.; Shur, M.L. *Modern Approaches to Simulation of Turbulence*; St. Petersburg Polytechnic University: Saint Petersburg, Russia, 2016. Available online: https://scholar.google.com/citations?view_op=view_citation&hl=ru&user=RegAS60AAAAJ&citation_for_view=RegAS60AAAAJ:dTyEYWd-f8wC (accessed on 24 March 2023).
42. Ferziger, J.H.; Peric, M. *Computational Methods for Fluid Dynamics*, 3rd ed.; Springer: Berlin/Heidelberg, Germany, 2002.
43. Smirnov, E.M.; Zaitsev, D.K. Finite volume method as applied to hydro- and gas dynamics and heat transfer problems in complex geometry domains. *St. Petersburg Polytech. Univ. J.* **2004**, *2*, 70–81.
44. Soloveychik, Y.G.; Royak, M.E.; Persova, M.G. *The Finite Element Method for Scalar and Vector Problems*; NSTU: Novosibirsk, Russia, 2007; ISBN 978-5-7782-0749.
45. Ozgen, S.; Canibek, M. Ice accretion simulation on multi-element airfoils using extended Messinger model. *Heat Mass Transfer.* **2008**, *45*, 305–322. [CrossRef]
46. Hedde, T. Modelisation Tridimensionnelle des Depots de Givre sur les Voilures D'aeronefs. Ph.D. Thesis, Universite Blaise-Pascal, Clermont-Ferrand II, France, 1992.
47. Messinger, B.L. Equilibrium temperature of an unheated icing surface as a function of airspeed. *J. Aeronaut Sci.* **1953**, *20*, 29–42. [CrossRef]
48. Jiao, X. Face offsetting: A unified approach for explicit moving interfaces. *J. Comp. Phys.* **2007**, *220*, 612–625. [CrossRef]
49. Koshelev, K.B.; Melnikova, V.G.; Strizhak, S.V. Development of iceFoam solver to simulate the icing process. *Proc. ISP RAS J.* **2020**, *32*, 217–234. [CrossRef] [PubMed]
50. Uyttersprot, L. Inverse Distance Weighting Mesh Deformation. A Robust and Efficient Method for Unstructured Meshes. Master's Thesis, Delft University of Technology Department of Aerodynamics, Brussels, Belgium, 12 February 2014; p. 177.
51. Ice accretion simulation // AGARD-AR-344.—1997. p. 280.
52. Radenac, E. Validation of a 3D ice accretion tool on swept wings of the SUNSET2 program, AIAA Aviation. In Proceedings of the 8th AIAA Atmospheric and Space Environments Conference, Washington, DC, USA, 13–17 June 2016.

53. Wright, B.W.; Rutkowski, A. Validation Results for LEWICE 2.0, NASA/CR--1999-208690. 1999. Available online: https://ntrs.nasa.gov/api/citations/19990021235/downloads/19990021235.pdf (accessed on 24 March 2023).
54. Yugulis, K.; Chase, D.; McCrink, M. Ice Accretion Analysis for the Development of the HeatCoat TM Electrothermal Ice Protection System. In Proceedings of the AIAA AVIATION 2020 Forum, Virtual Event, 15–19 June 2020. [CrossRef]
55. Shin, J.; Bond, T. Experimental and Computational Ice Shapes and Resulting Drag Increace for a NACA0012 Airfol. In Proceedings of the 5th Symposium on Numerical and Physical Aspects of Aerodynamic Flows Sponsored, California State University, Long Beach, CA, USA, 13-16 January 1992. NASA/TM-105743.
56. Heinrich, A.; Ross, R.; Zumwalt, G.; Provorse, J.; Padmanabhan, V.; Thompson, J.; Riley, J. *Aircraft Icing Handbook*; Federal Aviation Administration: Wichita, KS, USA, 1991.
57. Langmuir, I.; Blodgett, K. *A Mathematical Investigation of Water Droplet Trajectories*; Army Air Forces Technical Report 5418; Army Air Forces Headquarters, Air Technical Service Command, University of Illinois at Urbana-Champaign: Champaign, IL, USA, 1946.
58. Finstad, K.J. Numerical and Experimental Studies of Rime Ice Accretion on Cylinders and Airfoils. Ph.D. Thesis, University of Alberta, Edmonton, AB, Canada, 1986. [CrossRef]
59. Sokolov, P.; Virk, M.S. Droplet Distribution Spectrum Effects on Dry Ice Growth on Cylinders. *Cold Reg. Sci. Technol.* **2019**, *160*, 80–88. [CrossRef]